International Journal of Ocean and Coastal Engineering
Vol. 1, No. 3 (2018) 1850003 (17 pages)

DOI: 10.1142/S2529807018500033

Data Set of Wind–Waves Interactions in the Gulf of Aqaba

Almog Shani-Zerbib*
Faculty of Civil and Environmental Engineering,
Technion, Haifa 320003, Israel
almogsh@campus.technion.ac.il

Asaph Rivlin
IUI — The Interuniversity Institute for
Marine Sciences in Eilat, Eilat 88103, Israel
asaph.rivlin@mail.huji.ac.il

Dan Liberzon
Faculty of Civil and Environmental Engineering,
Technion, Haifa 320003, Israel
liberzon@technion.ac.il

Received 22 August 2018
Accepted 12 November 2018
Published 25 February 2019

A data set containing detailed measurements of wind velocity and wave fields, conducted in the Gulf of Aqaba, near the city of Eliat, is made freely available. The set is highly suitable to be used in students' education and specialists' training in the field of physical oceanography and wind–waves interactions. It contains measurements of the wind velocity field performed by two sonic anemometers, of water surface fluctuations conducted by a spatial array of staff wave gages, and of records of the water column pressure conducted by a submerged pressure gage. Recorded simultaneously at high temporal (80 Hz) and spatial resolutions, these data offer examination of various physical processes governing the wind–waves evolution. The diurnal fluctuations of the wind forcing allow examination of the wave field evolution during the growth, steady, and decay periods. Measured at two heights above the mean water level, wind velocity component records are suitable for deriving important wind flow characteristics. Examples of relevant processing methods and techniques are provided, including representative results, to serve as a reference point for educational use. These include estimations of the mean and fluctuating quantities and their daily variations, spectral analysis, and higher order statistical analysis.

Keywords: Educational data set; data set; wind–waves interactions; wave field evolution; wind forcing; Gulf of Aqaba; Gulf of Eliat.

*Corresponding author.

1. Introduction

A system of ocean waves excited by the wind and evolving under the wind forcing is one of the most intriguing and yet least-resolved environmental flows phenomena. Having a tremendous impact on daily human activities and playing a significant role in setting global and local climate, wind waves have been in the focus of the scientific community interest for many decades now. Yet after decades of experimental, theoretical, and numerical efforts, a comprehensive understanding of this phenomenon still eludes us. Although very simple at first glance, the coupled system of wind waves is actually very complex. The initially excited short water waves evolve, propagating and exhibiting some degree of directional distribution of energy, while being altered by the momentum and energy exchange with the wind turbulent boundary layer flow. Additionally, the wave field components interact with each other and are affected by the possible presence of currents and complex bathymetry. Some of the waves will elongate and grow in height during their evolution and some will break, redistributing their energy among other wave field components and contributing to the water kinetic energy (Babanin [2011]). Evolving in such complex process, the resulted wave field is analyzed using statistical approaches: waves energy density spectra and heights/troughs/crests exceedance probability distribution being among the most popular ways to describe the wave field state (Young [1999]; Janssen [2004]). A researcher working in the field of physical oceanography or an engineer performing design and maintenance tasks of maritime and coastal installations is required to possess a broad spectrum of knowledge and skills, such as fluid dynamics, physics, mathematics, scientific programing, and more. To meet this requirement, comprehensive education of undergraduate and graduate students on the topics of water waves and wind–waves interactions is taking place at universities and research institutions around the world. Alongside theoretical knowledge, practical approach is required to ensure that the trainees obtain the full grasp of the phenomena of interest. However, many educational institutes are lacking access to relevant laboratory facilities nor can they afford participating in costly open sea experiments. Aiming to fill this gap, results of recent open sea experiments, which took place in the Gulf of Aqaba, near the city of Eliat in Israel, are offered here mainly for educational and training purposes. For the best of our knowledge, this is the first data set containing detailed and high-resolution measurements of both the waves and the wind in the Gulf of Aqaba. The experiments were conducted as a part of a new graduate level advanced course focussing on water waves–wind interactions and are shared publicly to be used in educational classes and researchers training programs. The presented data sets contain records of the instantaneous water surface fluctuations performed by an array of wave gages, simultaneously recorded turbulent wind velocity fields at two altitudes, and records of the water column pressure variations. These data sets are highly suitable for education and training in modern data processing methods, mathematical analysis, presentation of results, etc. The sets are accompanied by

representative analysis results including mean wind velocity magnitude and direction, significant wave heights, wind profiles, wave heights, crests and troughs exceedance distribution functions (EDFs), and more, elaborating the extent of the data and serving as target examples.

2. Observation Site and Experimental Setup

The Gulf of Aqaba, located at the northern tip of the Red Sea, is highly suitable for conducting open sea wind waves studies as it offers relatively steady conditions in terms of wind direction and magnitude and humidity diurnal fluctuations throughout most of the year. Water temperature in the gulf varies from 20°C in the winter to 27°C in the summer (Biton and Gildor [2011]). Surrounded by two large mountain ridges, the Gulf of Aqaba experiences winds of moderate strength blowing at almost

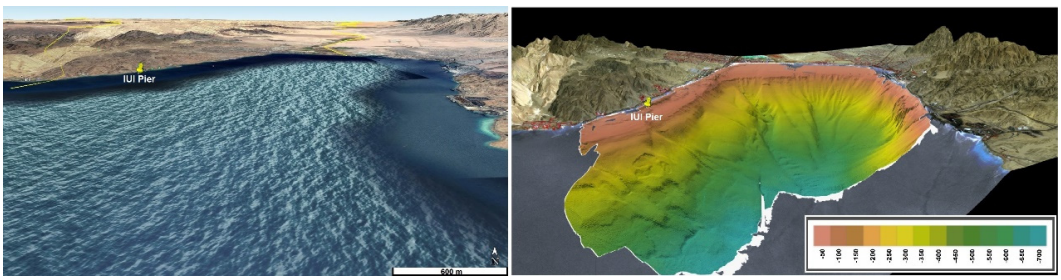

Fig. 1. Map and bathymetry of the Gulf of Aqaba and the measurement site (marked with the yellow pin).

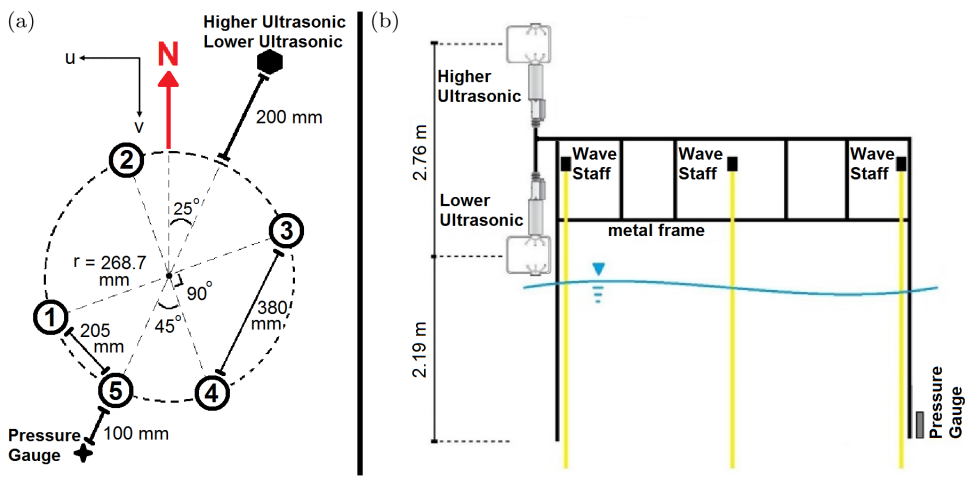

Fig. 2. (a) Overview of the wave gages array. All five wave gages (numbered circles) are located 268.7 mm from the center; the two ultrasonic anemometers (aimed toward north) and the water column pressure gage are marked by the hexagon and star, respectively. (b) Sideview of the instruments array with specified vertical separation between the Sonics and the water column pressure gage.

steady direction during the daylight hours, whereas during the night hours, the wind strength reduces to nearly zero.

Convenient wind regimes and elongated, close to rectangular, shape of the gulf resemble a laboratory wind wave flume setup, offering suitable environment for examining various stages of the fetch limited evolution of waves under forcing of the above blowing wind. The relatively slow diurnal variations of the wing forcing are convenient for examining the wave field response to changing wind forcing conditions during the morning and evening hours. The data sets presented here were collected continuously for over 50 h during June 2017 at the location of the Interuniversity Institute for Marine Sciences in Eilat (IUI-Eilat). The measurements began on June 11th at 9:32:55 and ended on June 13th at 13:15:08, which is the last data recorded in the last measurement data file. The measurements took place 2 m off the edge of a 40 m long pier (29°30.1084N and 34°55.0623E) at water depth of 4.5 m. The shoreline near the measurement site is aligned at about 45° east to the magnetic north (Figs. 1 and 2).

3. Instruments Array and Data Files

The instruments array was mounted on a large tripod resting on the seabed and was comprised of five capacitance-type water surface penetrating wave-staffs (*OSSI-010-002E-3 Wave-Staff*), one submerged pressure gage (*Keller PR-23 Y*), and two 3-D ultrasonic anemometers (*Young 81000*) hereafter referred to as Sonics. The lower anemometer was mounted up-side-down, and the recorded data orientation was adjusted accordingly during post-measurements processing. Instruments characteristics, including the records units, are detailed below in Table 1. The wave gages were arranged in a 2-D pentagon-shaped array, and the Sonics were positioned at 2.19 m

Table 1. List of instruments and data files parameters.

Instrument model	Measurement (notation)	Units	Accuracy	File naming pattern	Precision (number of digits after the decimal point)
Resistance-type wave-staff, *OSSI-010-002E-3*	Instantaneous water surface fluctuations, $\eta(t)$	m	±4.5 mm	*Waves_*	4
Submerged pressure gage, *Keller PR-23 Y*	Water column pressure, $p(t)$	Pa	± 100 Pa	*Pressure_*	3
3-D ultrasonic anemometer, *Young 81000*	Three Cartesian components of the turbulent wind flow at higher location ($u(t)$, $v(t)$, $w(t)$)	m/s	±0.05 m/sec	*SonicHigh_*	3
3-D ultrasonic anemometer, *Young 81000*	Three Cartesian components of the turbulent wind flow at lower location ($u(t)$, $v(t)$, $w(t)$)	m/s	±0.05 m/s	SonicLow_	3

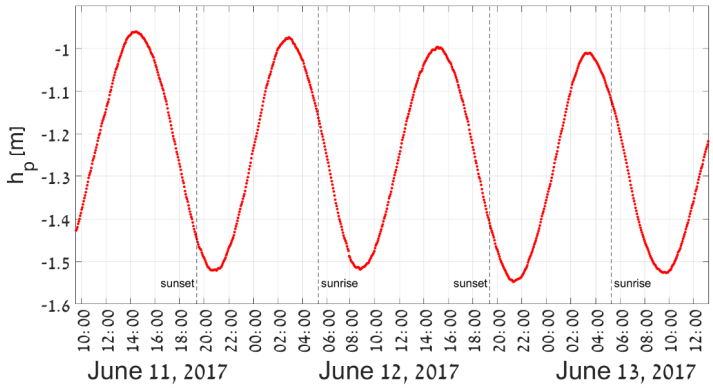

Fig. 3. Variations of the water column pressure depth $h_p(t)$.

and 4.95 m above the submerged water column pressure gage (Fig. 2). The actual elevation of the Sonics, relative to the mean water level (MWL), varied due to the tidal cycle. The average tidal amplitude was 0.27 [m] and was monitored by the pressure gage readings (Fig. 3). The Sonics were oriented to the magnetic north.

All sensors were configured to analog output and their respective signals were recorded simultaneously by a 16 bit analog-to-digital (A/D) card at 80 Hz and saved to a series of 204.8 s (2^{14} data points) long tab-delimited text files. All data were saved in physical units of water surface elevation m, wind velocity m/s, and water column pressure Pa. Wave gages output voltage-to-elevation conversion ratio was obtained by performing *a priori* calibration using sea water. The Sonics and the water column pressure gage voltage-to-velocity and voltage-to-pressure conversion ratios were provided by the respective manufacturers.

The naming pattern of data files begins with the type of measurement (Table 1), followed by a time stamp in the form of "... *_DD_MM_YYYY_hh_mm_ss*," all files have extension "*.dat*." Four different files were saved simultaneously: wave gages records containing five columns in each file (one for every gage data); pressure gage records in a single column; higher and lower ultrasonic anemometers records arranged in two separate files, each with three columns corresponding to the three Cartesian wind velocity field components. Precision of data records in the files varied according to the instrument type and is also detailed in Table 1.

All data are available for free educational and scientific use under the Creative Commons license. The data are stored at the Mendeley Data service under doi: 10.17632/kgx4559c67.2.

4. Example Data Processing and Results

As mentioned above, these data are freely distributed for educational and scientific research purposes. Below, we detail the recorded waves and wind characteristics in terms of mean and fluctuating parameters. We detail a number of possible processing

methods, including the implemented techniques, and where needed, the Matlab® code is used to complete these tasks. Matlab® code leading to creation of each of Figs. 3–9 is also included in the data as separate files named accordingly. Elaborate code explanations are given in each of the files, as well as the README file detailing all the codes provided. The results presented here are accompanied by an appropriate discussion in view of the meteorological conditions, developing wave field characteristics, wind–wave interactions, and more.

The below presented techniques and the results can be used as a reference target during the training in the relevant data processing techniques and discussion of the physical processes governing the wind–waves interactions. First, we resolve the MWL diurnal fluctuations due to the tidal cycle (Fig. 3). Data provided by the submerged water column pressure gage, $p_w(t)$, were used to calculate the gage depth $h_p(t)$ as:

$$h_p = -\frac{p_w}{\rho_w g}, \tag{1}$$

g being the gravitational constant and ρ_w denoting the sea water density value of 1,028 kg/m^3 (Biton *et al.* [2008]; Biton and Gildor [2011]). Knowing the vertical distance between each of the Sonics and the water column pressure gage, values of $h_p(t)$ were then used to determine the actual elevation values of the two Sonics above the MWL for each instance of time.

Next, the wind flow characteristics are examined. The wind flow was recorded by the two Sonics, each anemometer providing fluctuations of the three orthogonal wind velocity field components $u(t)$, $v(t)$, and $w(t)$ (for orientation see Fig. 2). To obtain representative magnitude and direction values, the time averaging of the wind velocity field components over the data set basic time periods of 204.8 s was performed, revealing very low mean vertical component values throughout the period of measurements. Hence, the time-averaged representative wind speed magnitude $\bar{U}$ and direction α, using the meteorological notation, can be obtained by:

$$|\bar{U}| = \sqrt{\bar{u}^2 + \bar{v}^2} \tag{2}$$

and

$$\alpha = \tan^{-1}\left|\frac{\bar{u}}{\bar{v}}\right|. \tag{3}$$

Fluctuations of both the mean wind speed magnitude and direction are presented in Fig. 4.

The observed wind regime exhibited clear diurnal variations. Periods of insignificant wind speed magnitude during the night hours were followed by an abrupt increase at sunrise. During the light hours, the wind regime exhibited a quasi-steady behavior characterized by mean wind speed values above 6 m/s. This quasi-steady period ended with gradual decrease of wind velocity at late afternoon hours, concluding the cycle with the wind speed dying out at sundown. During the quasi-steady

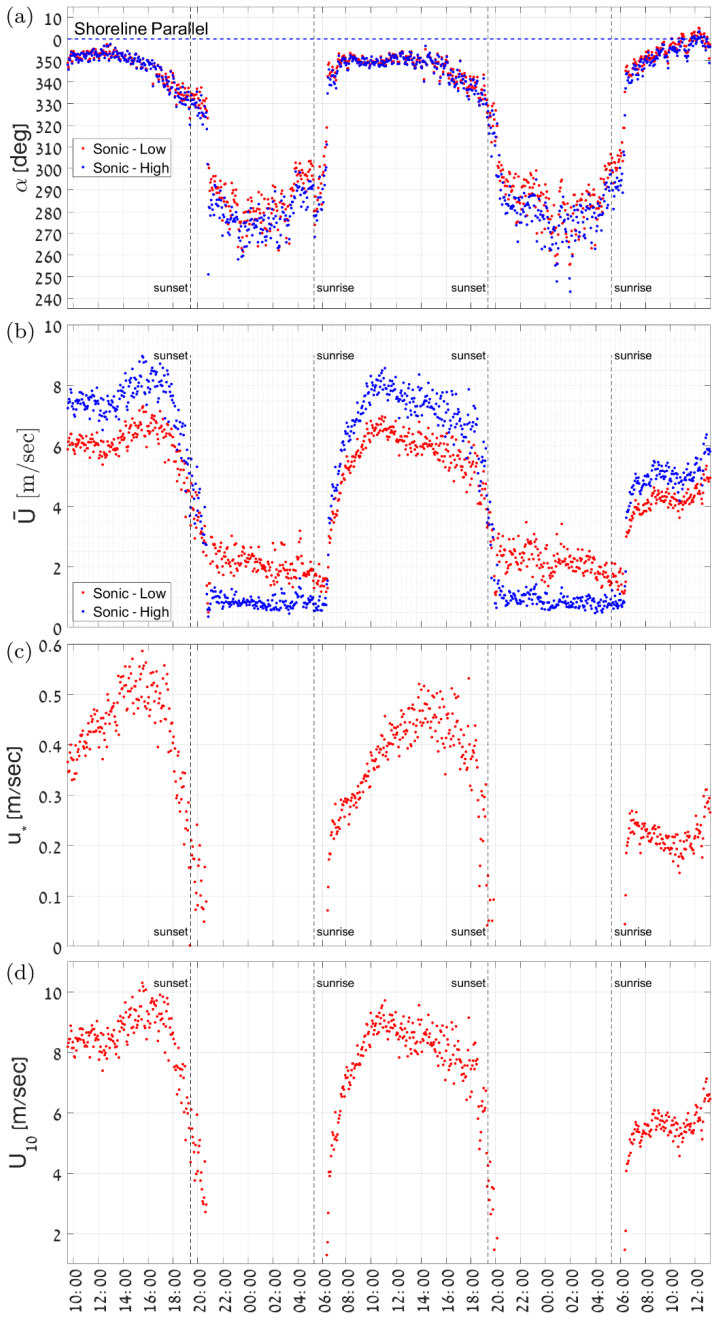

Fig. 4. Each dot in all plots represents an average of one data file (204.8 s); sunrise and sunset times are labeled and marked by the black dashed lines. (a) Wind direction as measured by higher (blue) and lower (red) Sonics; the shoreline parallel is marked by a blue dashed line at 0°. (b) Wind magnitude as measured by higher (blue) and lower (red) Sonics. (c) Friction velocity as calculated from logarithmic fit for significant wind magnitudes. (d) Wind magnitude at 10 m above the MWL, U_{10}, as calculated from logarithmic fit for significant wind magnitudes (color online).

period, when the wind speed reached maximum daily values, the wind direction was nearly constant at about 35° east. The shoreline orientation and bottom slope gradient at the measurement site have a profound impact on the water waves propagation direction. Therefore, the figures containing the wind speed and the waves propagation direction use coordinates system aligned with the shoreline, with the shoreline orientation line at 0°. Transformation from the meteorological coordinates system is achieved by a simple subtraction of 45° from the values calculated by Eq. (3).

The mean wind magnitude profile above the wavy water surface is assumed to be logarithmic:

$$\bar{U}(z) = \frac{u_*}{\kappa} \ln\left(\frac{z}{z_0}\right), \tag{4}$$

where $\kappa = 0.41$ is the Von Karman constant, u_* is the friction velocity, z is the height above the MWL, and z_0 is the representative water surface roughness as experienced by the wind boundary layer flow (Janssen [2004]; Schlichting and Gersten [2017]). Using the least-square fit method, the logarithmic profile (4) can be fitted to the Sonic provided data. Obtained from the fit, values of friction velocity and wind magnitude at 10 m above MWL, U_{10}, are also presented in Fig. 4.

The instantaneous water surface elevation fluctuations, $\eta(t)$, were measured by the five wave gages. Time series ensembles of surface elevation fluctuations, provided by each gage, allow time and spectral domain examination of the wave field. Use of two-dimensional array allows obtaining spatial characteristics of the wave field. Moreover, individual pairs of wave gages can be used to obtain wave field spectral component celerity values, which in turn allow derivation of the actual dispersion relation and its parametrization.

4.1. *Time domain*

Initial assessment of the measured wave field characteristics was required to determine adequate resolution and averaging periods for calculation of various parameters. For this, several power density spectra of $\eta(t)$ were calculated for different periods of the measurements. Such spectrum, for example, is given in Fig. 5 for one data file of the second day of measurement at noon, calculated at the highest available frequency resolution of 4.88E−3 Hz. Examination of the obtained spectra showed that the wind-generated wave energies were concentrated between 0.2 Hz and 1 Hz. Waves with dominant frequency values under 0.2 Hz are most likely bound waves caused by the finite width of the gulf. Considering this, there are two options to filter the measured data: (1) a bandpass filtering between 0.2 Hz and 1 Hz or (2) a lowpass filtering with the cutoff frequency of 1 Hz that results in inclusion of both bound and free waves generated by the wind. The difference between products of the two filtering options is shown in Fig. 6 in terms of mean wave period calculations.

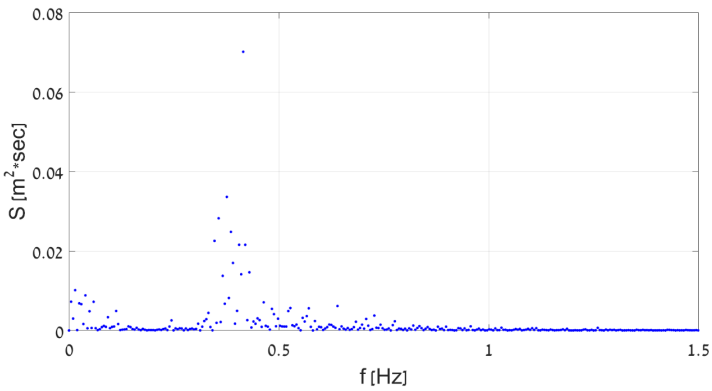

Fig. 5. $\eta(t)$ power density spectrum, one 204.8 s long data file on 12/06 at 12:01.

Observations of the wave field characteristics, showing dominant time periods of 2.5–3.5 s and wind magnitude and direction change rates, allow determination of optimal averaging periods to produce meaningful statistical analysis of the data. While considering longer averaging periods is essential for having a correct statistical representation of the examined phenomena, excessive length of averaging periods will inevitably lead to omission of variations in various calculated characteristics and other quantities. Aiming at having at least 10 different analysis segments covering wind characteristic variations during the morning and evening changes, spanning roughly 2–3 h each, predestines averaging over ensembles of roughly 15 min. Shorter ensembles produce results overridden by noise due to short time fluctuations, whereas using larger ensembles smoothens the results causing obstruction in evaluating the examined phenomena variations. Selecting averaging ensembles to be 15 min long, instantaneous fluctuations of the water surface elevation, $\eta(t)$, were processed implementing the zero-crossing method, collecting ensembles of crest, trough, and wave height values. Values of H_s were then calculated for each ensemble as the average of the highest 1/3 wave height values (Dean and Dalrymple [1991]). Variations of the significant wave height H_s and of the mean wave period T_m along the time period of measurements are presented in Fig. 6 for both bandpass and lowpass filtering, as described earlier. It is noticeable that the difference in H_s values between bandpass and lowpass filtering, shown in Fig. 6(a) and Fig. 6(c), is insignificant. However, using bandpass filtering omits the longer waves, as shown in the first day afternoon in Fig. 6(d). Variations of H_s exhibited strong correlation with those of the mean wind magnitude and direction. Generally, the significant wave height increased almost simultaneously with the increase in the mean wind speed (Fig. 4(b)). While during the second day of measurements, the wind speed variations did not exhibit significant fluctuations beside the initial morning increase and the eventual evening decay, during the first day the mean wind speed has exhibited a temporarily decrease between 11:00 and 14:00. It was followed by an increase of the mean wind speed lasting until the eventual evening hours decay. The second peak during the late

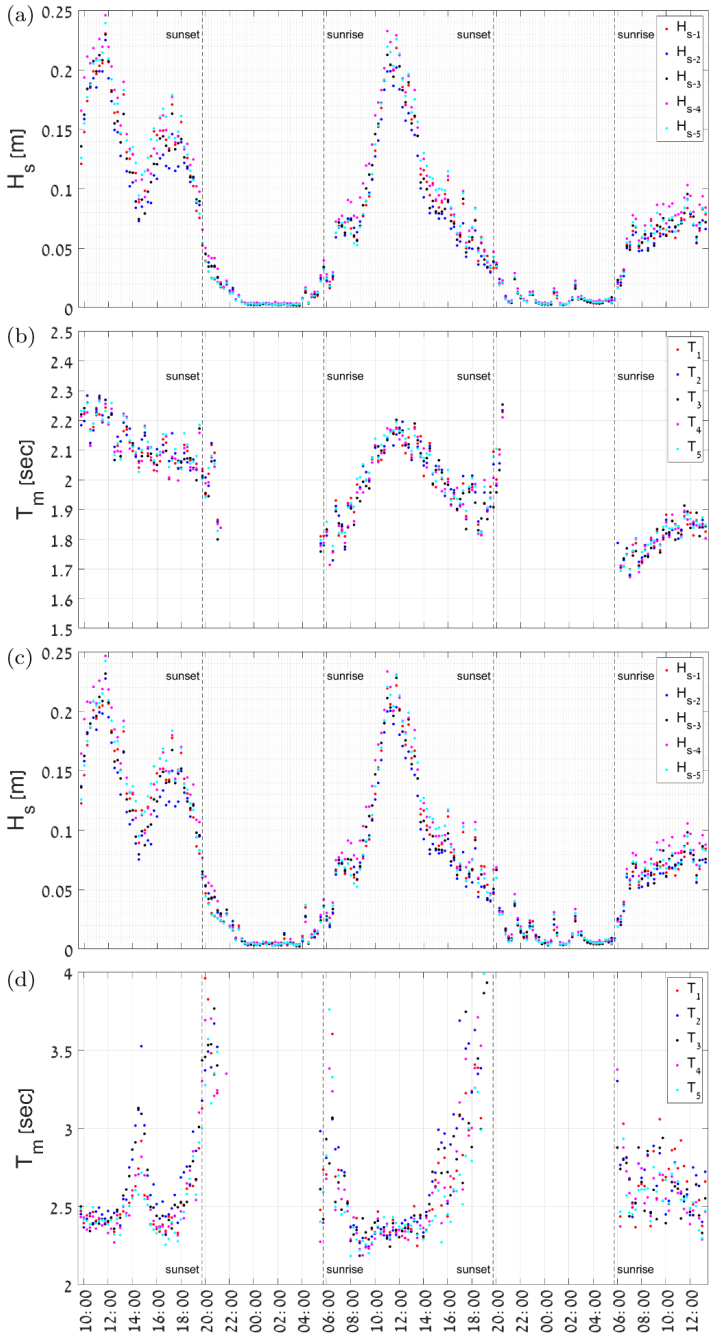

Fig. 6. 15 min averages of all five wave gages filtered data from zero-cross analysis. (a) Averaged significant wave height after bandpass filtering in the range 0.2–1 Hz. (b) Averaged time period after bandpass filtering in the range 0.2–1 Hz for time periods corresponding $H_s > 0.02$ m. (c) Averaged significant wave height after lowpass filtering at 1 Hz. (d) Averaged time period after lowpass filtering at 1 Hz for time periods corresponding $Hs > 0.02$ m.

afternoon hours was accompanied also by a change in wind direction, gradually shifting toward 15° north. Such variation in both wind speed and direction triggered a significant wave field response. The wave height values became larger, whereas the mean time period decreased slightly. Visual observations of the wave field, performed at the site of measurements, also indicated increased number of breaking occurrences at that time. Influence of the long waves, as seen in these plots, can be effectively eliminated by using a bandpass filtering or alternatively by implementing a bound waves removing algorithm described in Fedele *et al.* [2010].

4.2. *Spatial characteristics of the wave field*

Spatial characteristics of the measured wave field can be obtained using one of several modern methods, such as the direct Fourier transformation method (Barber [1961]), the maximum likelihood method (Capon [1969]), or the extended maximum entropy principle (Hashimoto [1997]). An extensive summary of the directional spectrum estimation methods can be found in Hashimoto [1997]. Here, we choose to demonstrate the use of the wavelet directional method (WDM), originally developed by Donelan *et al.* [1996], as it recently gains popularity (e.g. Hauser *et al.* [2005]; Laxague *et al.* [2015]; Rapizo *et al.* [2016]; Toffoli *et al.* [2017]). The Matlab® code was freely shared by the original authors and is included among the data set files. WDM considers the observed groupness of the wave field and uses the Morlet mother wavelet to describe the wind-generated waves. Detailed instructions regarding the inputs and the expected products can be found in the original README file, also available alongside the code. The results of WDM (Fig. 7) were bound to frequency range of 0.2–2 Hz; the number of voices for the wavelet transform was chosen to be 12. Polar representation of the used wave gages array, as required by the WDM, was derived setting the center of the coordinate system ($r = 0$, $\varnothing = 0$) at the center of the array (Fig. 2), so all five wave gages were positioned at $r = 0.2687$ m. The polar axis is

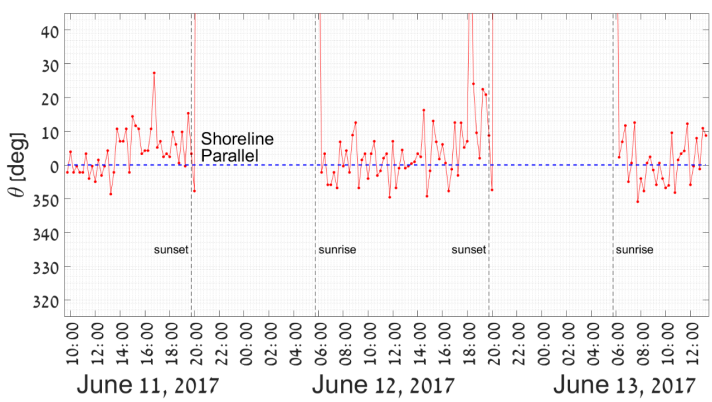

Fig. 7. Average direction of the wave field energy propagation direction of 15 min data sets; 0° denotes waves propagating along the shoreline parallel, marked by the horizontal dashed line (color online).

oriented toward the east and the angle increases counterclockwise; therefore, the azimuth angles of the wave gages (in ascending order, from wave gage number one to wave gage number five) are $\emptyset = [(20\pi/18), (11\pi/18), (2\pi/18), (29\pi/18), (49\pi/36)]$. The output is the directional spread of the wave field energy propagation, corresponding to the same coordinate system. In Fig. 7, the waves propagation direction is presented in the shoreline parallel coordinates system, matching that of Fig. 4(a). The mean propagation direction of the wave field was found by considering only time periods of significant wind magnitude, i.e. U_{10} values higher than 1 m/s. Wind magnitude during the night was insignificant. An average of ensembles of $\eta(t)$, each 15 min long of four to five consecutive data files from 6:00 to 20:00, was used to obtain the estimated propagation direction (denoted as θ in Fig. 7).

The daily mean waves energy propagation direction, immediately after the wind speed increases during the early morning hours, was observed to be about 45° north, i.e. along the shoreline parallel. It then slowly shifted away from the shoreline parallel at sunset, accompanied by the decrease of the mean wind speed.

4.3. *Spectral analysis and higher order statistics*

In this section, various spectral characteristics of the measured wave field are discussed, and the surface elevation data are examined in view of higher order exceedance probability distribution models. The power density spectra of the instantaneous water surface elevation fluctuations were obtained by applying windowed averaged Fourier transform. For each 204.8 sec long ensemble of $\eta(t)$ contained in one data file, windows of 2^{13} data points (102.4 s long) were used, with 50% overlapping, resulting in frequency resolution of $9.765 * 10^{-3}$ Hz.

Detailed surface elevation fluctuation power density spectra of all data are not presented here due to space constraints. Examining variations of the wave field energy in terms of the significant wave height (Fig. 6), three periods corresponding to the growth, steady, and decay stages of the wave field evolution were identified. Here, Fig. 8 presents three representative normalized spectral shapes corresponding to the three typical stages of wave field evolution. The presented spectra were normalized by their respective peak of surface elevation fluctuations energy power density and the corresponding frequency values. Such presentation allows easy comparison of spectral shapes basic characteristics, such as the spectral width, asymmetry between the long and the short waves sides of the spectrum, and the high frequencies tail decay rates. The latter is seen to increase in the representative spectral shapes as the wave field evolution stage changes from growth to steady to decay. Spectra of all three stages exhibited the expected JONSWAP-like shape (Hasselmann *et al.* [1973]; Janssen [2004]) with steeper low frequencies side, while during the decay stage the spectrum shape asymmetry is the smallest.

The EDFs were calculated for representative data sets corresponding to the three stages of the wave field evolution. For each stage representative data set, each

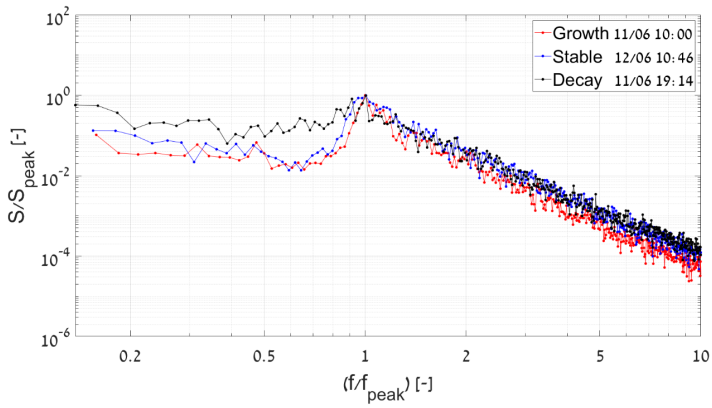

Fig. 8. Normalized power density spectra of the water surface elevation fluctuations during representative periods corresponding to the three stages of the wave field evolution: growth stage on 11/06/17 at 10:00–10:14 (red); steady stage on 12/06/17 at 10:46–11:00 (blue); decay stage on 11/06/17 at 19:14–19:28 (black) (color online).

approximately 15 min long was selected: on 12/6/2017 at 10:46 to 11:00 for steady, on 11/6/2017 at 10:00 to 10:14 for growth, on 11/6/2017 at 19:14 to 19:28 for decay stage. Before processing the time series of the surface elevation fluctuations, the data were band pass-filtered in the range between 0.2 Hz and 1 Hz. The root mean square (RMS) of the filtered signals, σ, was used for normalization, and all normalized parameters below are denoted by the σ subscript. Sorted lists of wave heights, crests, and troughs were constructed using the zero-crossing method, and probabilities of exceedance were calculated for all ensembles. The EDFs were compared against the Rayleigh wave height probability distribution, defined as:

$$P_R = e^{-\left(\frac{H_\sigma^2}{8}\right)}, \tag{5}$$

where H_σ is the normalized (by RMS) wave height and P_R is the probability to exceed H_σ. EDFs of the Tayfun–Fedele model of the third order, TF3 (Tayfun and Fedele [2007]), were also obtained and are presented in Fig. 9. To calculate the third-order correction of the TF3 model, Λ, the fourth-order joint cumulants λ_{mn}, for which $m + n = 4$, were obtained from

$$\lambda_{mn} = \frac{\overline{\eta^m \hat{\eta}^n}}{\sigma^{m+n}} + (-1)^{\frac{m}{2}}(m-1)(n-1). \tag{6}$$

Here, η and $\hat{\eta}$ have a 90° phase shift between them and overbar denotes ensemble averaging. The joint cumulants take form of

$$\Lambda = \lambda_{40} + 2 \cdot \lambda_{22} + \lambda_{04}. \tag{7}$$

The third-order correction is then used to calculate the EDF of the wave height distribution:

$$E_H(H_\sigma) = e^{-\left(\frac{H_\sigma^2}{8}\right)}\left[1 + \frac{\Lambda}{1024} H_\sigma^2 (H_\sigma^2 - 16)\right]. \tag{8}$$

To express the effect of second-order nonlinearities that cause the asymmetry in the wave envelope, in terms of higher crests and shallower troughs,

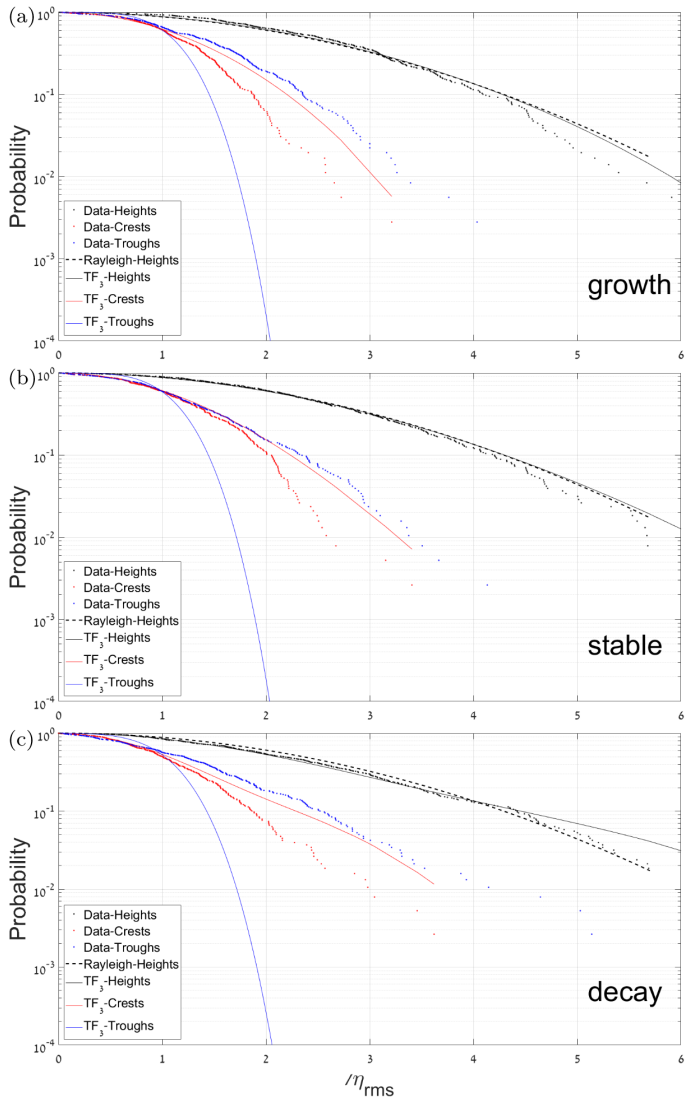

Fig. 9. EDFs of wave heights (black), crests (red), and troughs (blue) ensembles of 15 min long data sets. The measurements data are the black dots, TF3 model results are the solid curves, and Rayleigh distribution for wave heights ensembles is the black dashed curve. Wave field evolution: (a) growth stage; (b) steady stage; (c) decay stage (color online).

we use μ^*:

$$\mu^* = 16\frac{A_2^3}{B_2}\Gamma\left(\frac{3}{B_2}\right) - \frac{1}{4}\sqrt{\frac{\pi}{2}}, \tag{9}$$

where Γ is the gamma function. A_2 and B_2 are defined in Forristall [2000]:

$$A_2 = 0.3536 + 0.2892\left(\frac{2\pi}{g}\frac{4\sqrt{m_0}}{T_1^2}\right) + 0.106\left(\frac{4\sqrt{m_0}}{k_1^2 h^3}\right), \tag{10}$$

$$B_2 = 2 - 2.1597\left(\frac{2\pi}{g}\frac{4\sqrt{m_0}}{T_1^2}\right) + 0.0968\left(\frac{4\sqrt{m_0}}{k_1^2 h^3}\right)^2, \tag{11}$$

where m_0 is the zero-order spectral moment, T_1 is the mean wave period calculated from the spectral moments (Tucker and Pitt [2001]), k_1 is the wavenumber for the frequency $1/T_1$, and h is the water depth. EDFs of both crest and trough distributions are then attained by

$$E_{\eta_{c-\sigma}} = \exp\left[-\frac{1}{2}\left(\frac{-1+\sqrt{1+2\cdot\mu^*\cdot\eta_{c-\sigma}}}{\mu^*}\right)^2\right]\left[1+\frac{\Lambda}{64}\eta_{c-\sigma}^2(\eta_{c-\sigma}^2-4)\right], \tag{12}$$

$$E_{\eta_{t-\sigma}} = \exp\left[-\frac{\eta_{t-\sigma}^2}{2}\left(1+\frac{\mu^*\cdot\eta_{t-\sigma}}{2}\right)^2\right]\left[1+\frac{\Lambda}{64}\eta_{t-\sigma}^2(\eta_{t-\sigma}^2-4)\right]. \tag{13}$$

The TF3 function results are similar to those predicted by Rayleigh distribution during the growth and steady stages of evolution, while exhibiting significant deviations during the decay stage. For all stages of the wave field evolution, the TF3 model fails to predict distribution of troughs by significantly underpredicting the actual measured distribution. However, the TF3 model performs better for crests distribution. Another interesting result seen in Fig. 9 is that while closely following the crests distribution during the steady stage, the measured troughs EDF is larger than that of the crests during the growth and steady stages and is smaller during some of the decay stage. Such changes indicate significant changes in the actual waves vertical asymmetry between the various stages of the examined fetch-limited evolution under the wind forcing.

5. Conclusions

The presented experimental data set, containing wind and waves data from the open sea measurements, is distributed freely with the aim to support the practical side of education of marine engineers, oceanographers, and other related scientific and engineering programs covering the topics of wind–waves interactions. The set, collected at the Gulf of Aqaba, contains more than 50 h of continuous measurements of the instantaneous water surface elevation performed by a spatial array of water-penetrating gages, wind velocity field fluctuations recorded at two heights above the mean water

surface, and the water column pressure data used to derive the wind measurements actual elevations relative to the MWL. The nature of the wind forcing experienced at the site of measurements, exhibiting diurnal variations and including periods of wind increase and decay with prolonged periods of steady wind forcing during the midday hours, rendering these data as highly suitable for studying the fetch-limited evolution of the wave field under varying and steady wind forcing conditions. The high-frequency resolution and the use of spatial array of wave gages allow implementation of various time and frequency domain calculation methods to derive important parameters of the physical processes involved in the wave field temporal evolution under wind forcing. Simultaneous measurements of all components of the wind velocity field at two elevations allow investigation of the wind–waves interactions and examination of wind flow characteristics in terms of mean and fluctuating quantities. The data set is accompanied by selective processing examples and representative results that will allow comparison and can serve as reference targets during the educational process.

Acknowledgments

The work presented here was supported by the ISF Grant 1521/15. The authors express their appreciation to the IUI staff for technical support.

References

Babanin, A. V. [2011] *Breaking and Dissipation of Ocean Surface Waves*, 1st edn (Cambridge University Press, NY, USA), 463pp.

Barber, N. F. [1961] "The directional resolving power of an array of wave detectors," *Ocean Wave Spectra*, Englewood Cliffs, N. J. Prentice Hall Inc, pp. 137–150.

Biton, E. & Gildor, H. [2011] "The general circulation of the Gulf of Aqaba (Gulf of Eilat) revisited: The interplay between the exchange flow through the Straits of Tiran and surface fluxes," *J. Geophys. Res. Ocean* **116**, 1–15, doi: 10.1029/2010JC006860.

Biton, E., Silverman, J. & Gildor, H. [2008] "Observations and modeling of a pulsating density current," *Geophys. Res. Lett.* **35**, 1–5, doi: 10.1029/2008GL034123.

Capon, J. [1969] "High-resolution frequency-wavenumber spectrum analysis," *Proc. IEEE* **57**, 1408–1418, doi: 10.1109/PROC.1969.7278, https://ieeexplore.ieee.org/abstract/document/1449208/.

Dean, R. & Dalrymple, R. [1991] *Water Wave Mechanics for Engineers and Scientists* (World Scientific, Singapore), pp. 1–353.

Donelan, M. A., Drennan, W. M. & Magnusson, A. K. [1996] "Nonstationary analysis of the directional properties of propagating waves," *J. Phys. Oceanogr.* **26**, 1901–1914, doi: https://doi.org/10.1175/1520-0485(1996)026<1901:NAOTDP>2.0.CO;2.

Fedele, F., Cherneva, Z., Tayfun, M. A. & Guedes Soares, C. [2010] "Nonlinear Schrödinger invariants wave statistics," *Phys. Fluids* **22**, 1–10, doi: 10.1063/1.3325585.

Forristall, G. Z. [2000] "Wave crest distributions: Observations and second-order theory," *J. Phys. Oceanogr.* **30**, 1931–1943, doi: 10.1175/1520-0485(2000)030<1931:WCDOAS>2.0.CO;2, http://journals.ametsoc.org/doi/abs/10.1175/1520-0485%282000%29030%3C1931%3AWCDOAS%3E2.0.CO%3B2.

Hashimoto, N. [1997] "Analysis of the directional wave spectrum from field data," *Adv. Coast. Ocean Eng.* **3**, 103–143.

Hasselmann, K. *et al.* [1973] "Measurements of wind-wave growth and swell decay during the Joint North Sea Wave Project (JONSWAP)," *Ergnzungsh. zur Dtsch. Hydrogr. Zeitschrift R.* **A(8)**, 95, doi:citeulike-article-id:2710264.

Hauser, D., Kahma, K. & Krogstad, H. E. [2005] Measuring and analyzing the directional spectra of ocean waves, http://www.envia.bl.uk//handle/123456789/4300.

Janssen, P. [2004] *The Interaction of Ocean Waves and Wind* (Cambridge University Press, NY, USA).

Laxague, N. J. M., Haus, B. K., Bogucki, D. & Özgökmen, T. [2015] "Spectral characterization of fine-scale wind waves using shipboard optical polarimetry," *J. Geophys. Res. Ocean* **120**, 3140–3156, doi: 10.1002/2014JC010403.

Rapizo, H., Waseda, T., Babanin, A. V. & Toffoli, A. [2016] "Laboratory experiments on the effects of a variable current field on the spectral geometry of water waves," *J. Phys. Oceanogr.* **46**, 2695–2717, doi: 10.1175/JPO-D-16-0011.1, http://journals.ametsoc.org/doi/10.1175/JPO-D-16-0011.1.

Schlichting, H. & Gersten, K. [2017] *Boundary Layer Theory*, 9th edn. (Springer-Verlag, NY, USA), pp. 1–805.

Tayfun, M. A. & Fedele, F. [2007] "Wave-height distributions and nonlinear effects," *Ocean Eng.* **34**, 1631–1649, doi: 10.1016/j.oceaneng.2006.11.006.

Toffoli, A. *et al.* [2017] "Wind generated rogue waves in an annular wave flume," *Phys. Rev. Lett.* **118**, 144503–144508.

Tucker, M. J. & Pitt, E. G. [2001] "Waves in ocean engineering," Vol. 5, Elsevier Science, LTD, Oxford, UK.

Young, I. R. [1999] *Wind Generated Ocean Waves*, 1st edn. Elsevier Science, LTD, Oxford, UK, 288pp.